On the development of three-dimensional vortex breakdown in cylindrical regions

M. A. Herrada
Escuela Superior de Ingenieros, Universidad de Sevilla, Camino de los Descubrimientos s/n, Sevilla 41092, Spain

R. Fernandez-Feria
E. T. S. Ingenieros Industriales, Universidad de Málaga, Pza. El Ejido s/n, Málaga 29013, Spain

(Received 20 October 2005; accepted 25 July 2006; published online 25 August 2006)

Three-dimensional and axisymmetric numerical simulations of the incompressible Navier-Stokes equations have been conducted to study the appearance and development of vortex breakdown in a family of columnar vortex flows in a straight pipe without wall friction. The numerical simulations show that the basic form of breakdown is axisymmetric, and a transition to helical breakdown modes is shown to be caused by a sufficiently large pocket of absolute instability inside the original axisymmetric "bubble" of recirculating flow. Depending on the values of the Reynolds and swirl parameters, two distinct unstable modes corresponding to azimuthal wave numbers $n=+1$ and $n=+2$ have been found to yield a helical or a double-helical breakdown mode, respectively. By means of a simple linear spatial stability analysis carried out in the sections of the pipe where the basic axisymmetric flow presents reverse flow, we have identified the frequencies and the dominant azimuthal wave numbers observed in the three-dimensional simulations. © *2006 American Institute of Physics*. [DOI: 10.1063/1.2338065]

I. INTRODUCTION

Vortex breakdown has been described as a catastrophic structural change in the flow of intense vortex cores by Hall.[1] Several breakdown patterns ranging from asymmetric spiral vortex cores to almost axisymmetric stagnant bubbles have been observed; in addition, unsteadiness of the flow and turbulence usually develop in the wake downstream the breakdown zone (see, e.g., Refs. 2–5, among many others). The prediction and control of vortex breakdown in either swirling flows in pipes or in unconfined vortices are of interest in many engineering applications: vortex cores over delta wings at high incidence angles, wing trailing vortices, swirling flows inside pipes and other swirl devices, combustion chambers, etc.

There is a large number of numerical studies which have analyzed the occurrence of this phenomenon in axisymmetric swirling flows in pipes. Some of them are inviscid analysis,[6–8] while other ones pay special attention to the role of viscosity,[9,10] or to the compressibility effects.[11,12] However, although experiments on vortex breakdown reveal the three-dimensional (3D) character of the phenomenon in most cases studied, very few theoretical or numerical works dealing with nonaxisymmetric swirling flows have been carried out. In the context of swirling flows in pipes, Tromp and Beran[13] studied the temporal evolution of a compressible, swirling, 3D flow in a pipe for values of the Reynolds and Mach numbers equal to 1000 and 0.3, respectively. More recently, and in the context of open flows, Ruith *et al.*[14] have extensively studied the three-dimensional vortex breakdown of incompressible swirling jets and wakes. These authors, who considered a two-parameter family of velocity profiles, found out that these swirling flows exhibited, in the absence of external co-flow, helical or double-helical breakdown modes for sufficiently high Reynolds and swirl numbers. In particular, they found that the basic form of breakdown is axisymmetric, and suggested that the asymmetric (helical or double helical) breakdown was related to the existence of a sufficiently large pocket of absolute instability in the wake of the recirculating bubble, corresponding to helicoidal modes with azimuthal wave numbers $m=-1$ and $m=-2$, respectively, where "the minus sign represents the fact that the winding sense of the spiral is opposite to that of the flow." This sign convention of the azimuthal wave number in Ref. 14 is not the one generally used in the normal mode decomposition, where $m<0$ means winding with the jet.[15] Some of the findings by Ruith *et al.* were subsequently confirmed experimentally for swirling jets by Liang and Maxworthy.[16]

In this paper, we have conducted both axisymmetric and 3D numerical simulations to study the appearance of vortex breakdown in a family of columnar vortex flows in straight pipes (without wall friction). In particular, our main interest is to know whether the three-dimensional (helical or double-helical) form of vortex breakdown inside a pipe is a phenomenon of the same kind as the axisymmetric vortex breakdown, or it develops from instabilities of the axisymmetric (recirculating bubble) vortex breakdown. To that end, the numerical results have been complemented with a local stability analysis of the axisymmetric swirling flows after a recirculating bubble has been formed. Following the ideas developed by Pier and Huerre[17,18] in the case of developing wake flows, but using the criterion for frequency selection given by Pierrehumbert[19] in the context of baroclinic instabilities, we have looked for regions of absolute instability inside the recirculating bubble (see also Gallaire *et al.*[20] for a

recent work on a similar problem). The stability results have been compared to the 3D numerical simulations in order to try to identify the frequencies and the dominant azimuthal wave numbers observed in the 3D simulations.

The paper is organized as follows: Sec. II contains the equations and the initial and boundary conditions of the problem. In particular, we consider the time evolution of a family of columnar swirling flows of Batchelor-type in a straight pipe. The numerical scheme for the integration of the full incompressible Navier-Stokes equations is given in Sec. III. Numerical results, both axisymmetric and 3D, are given and discussed in Sec. IV. A linear, spatial stability analysis of the axisymmetric flow is given in Sec. V. Finally, results are discussed and summarized in Sec. VI.

II. FORMULATION OF THE PROBLEM

In the present paper, the incompressible, time-dependent and three dimensional Navier-Stokes equations are solved in cylindrical coordinates $(r,\ \theta,\ z)$ inside a pipe. To render the governing equations dimensionless, a characteristic length δ, and a characteristic velocity w_c, are introduced. As we will see later, both quantities are defined at the pipe entrance and characterize the inlet columnar vortex, being δ the characteristic vortex core radius, and w_c the velocity at the axis of the tube. The convective time scale is $T=\delta/w_c$, and the characteristic pressure is $P=\rho w_c^2$, with ρ representing the constant density of the fluid. With this scaling, the dimensionless continuity and momentum equations can be written as

$$\frac{1}{r}\frac{\partial(ru)}{\partial r}+\frac{\partial w}{\partial z}+\frac{1}{r}\frac{\partial v}{\partial\theta}=0, \tag{1}$$

$$\frac{Du}{Dt}=-\frac{\partial p}{\partial r}+\frac{v^2}{r}+\frac{1}{\mathrm{Re}}\left[\nabla^2 u-\frac{u}{r^2}-\frac{2}{r^2}\frac{\partial v}{\partial\theta}\right], \tag{2}$$

$$\frac{Dv}{Dt}=-\frac{1}{r}\frac{\partial p}{\partial\theta}+\frac{uv}{r}+\frac{1}{\mathrm{Re}}\left[\nabla^2 v-\frac{v}{r^2}+\frac{2}{r^2}\frac{\partial u}{\partial\theta}\right], \tag{3}$$

$$\frac{Dw}{Dt}=-\frac{\partial p}{\partial z}+\frac{1}{\mathrm{Re}}[\nabla^2 w], \tag{4}$$

where (u,v,w) and p are the dimensionless velocity and pressure fields, respectively, and the mathematical operators D/Dt and ∇^2 are

$$\frac{D}{Dt}=\frac{\partial}{\partial t}+u\frac{\partial}{\partial r}+w\frac{\partial}{\partial z}+\frac{v}{r}\frac{\partial}{\partial\theta} \tag{5}$$

and

$$\nabla^2=\frac{1}{r}\frac{\partial}{\partial r}\left(r\frac{\partial}{\partial r}\right)+\frac{\partial^2}{\partial z^2}+\frac{1}{r^2}\frac{\partial^2}{\partial\theta^2}. \tag{6}$$

The Reynolds number is defined as

$$\mathrm{Re}=\frac{w_c\delta}{\nu} \tag{7}$$

being ν the kinematic viscosity of the fluid.

The above system of equations has been solved to describe the temporal evolution of a family of columnar swirling flows in a straight pipe, which in dimensionless form are given by the following expressions:

$$w=a+(1-a)\exp(-r^2),\quad v=\frac{S}{r}[1-\exp(-r^2)],\quad u=0, \tag{8}$$

where parameter $a\equiv w_\infty/w_c$ is the ratio between the axial velocity far away from the axis, w_∞, and the velocity at the axis, w_c, used as the characteristic velocity; S is a swirl parameter, defined as

$$S=\frac{\Gamma}{\delta w_c}, \tag{9}$$

being Γ the circulation of the vortex far away from the axis. Note that all the exponentials terms appearing in (8) are of order unity when $r\sim 1$, which corresponds to a dimensional radial distance of order δ, so that δ is the characteristic vortex core radius. This kind of velocity profile, combination of an axial flow (jet-like for $a<1$ and wake-like for $a>1$) and a circumferential (Burger's vortex) flow, with no radial flow, fits well with the inlet velocity of some experiments on vortex breakdown in pipes.[21] It is sometimes called Batchelor vortex, and has been extensively used in different theoretical and numerical investigations of axisymmetric swirling flows in pipes,[6,12] in addition to the original modelling of aircraft trailing vortices.[22,23]

This axisymmetric velocity field (8) will be used here as the initial condition for both the axisymmetric numerical simulations (neglecting the azimuthal derivatives in the equations) and some of the 3D computations reported below. In addition, the steady state axisymmetric solutions resulting from the axisymmetric computations (when they exist) will also be used as initial conditions in the rest of the 3D numerical simulations performed in this work (see Sec. VI).

We have considered the following set of boundary conditions:

- At the inlet section, $z=0$, we assumed that the velocity profiles given by Eq. (8) remain unaffected during the time evolution of the flow.
- At the outlet section, $z=z_f$, zero gradient outflow conditions have been imposed to the velocity field.
- The pipe wall, $r=R_o$, is treated as an inviscid stream surface, so that impermeability is enforced at this boundary, but allowing velocity slip. Thus the wall is assumed to be a steady, axisymmetric stream surface at which circulation, $\Gamma=rv$, and azimuthal vorticity, $\eta=u_z-w_r$, remain constant and equal to the given values at the pipe entrance,

$$\frac{\partial w}{\partial r}=u=0,\quad v=\frac{S}{R_o}[1-\exp(-R_o^2)]\simeq\frac{S}{R_o}. \tag{10}$$

This type of inviscid boundary condition at the pipe wall has been widely used in the past in problems dealing with vortex breakdown in tubes.[9,10] It greatly simplifies the numerical treatment of the problem. Although the wall boundary layer

may have a significant impact on the flow behavior if the boundary layer thickness grows too much, it is generally assumed that it is not important in describing the genesis of vortex breakdown. The calculations are carried out with a fixed geometric characterized by $R_o=4$ and $z_f=60$.

III. COMPUTATIONAL METHOD

Since the flow must be 2π periodic in θ, the velocity field, $\mathbf{u}=(u,v,w)$ can be projected exactly onto a set of two-dimensional complex Fourier modes $\hat{\mathbf{u}}_n$ as

$$\mathbf{u}(z,r,\theta,t)=\sum_{n=-\infty}^{\infty}\hat{\mathbf{u}}_n(z,r,t)\exp(in\theta). \tag{11}$$

We introduce the following notation for the gradient and Laplacian of a (complex) scalar, as applied to mode n of the Fourier decomposition:

$$\nabla_n=\left(\partial_z,\partial_r,\frac{in}{r}\right),\quad \nabla_n^2=\partial_z^2+\frac{1}{r}\partial_r(r\partial_r)-\frac{n^2}{r^2}=\nabla_{rz}^2-\frac{n^2}{r^2}. \tag{12}$$

The change of variables $\tilde{u}_n=\hat{u}_n+i\hat{v}_n$, $\tilde{v}_n=\hat{u}_n-i\hat{v}_n$, is introduced to decouple the linear terms in the equations.[24] Then, the cylindrical components of the transformed momentum equation read

$$\partial_t\tilde{u}_n+\widetilde{\mathbf{N}(\mathbf{u})}_{zn}=-\left(\partial_r-\frac{n}{r}\right)\hat{p}_n+\frac{1}{\mathrm{Re}}\left(\nabla_{rz}^2-\frac{[n+1]^2}{r^2}\right)\tilde{u}_n, \tag{13}$$

$$\partial_t\tilde{v}_n+\widetilde{\mathbf{N}(\mathbf{u})}_{\theta n}=-\left(\partial_r+\frac{n}{r}\right)\hat{p}_n+\frac{1}{\mathrm{Re}}\left(\nabla_{rz}^2-\frac{[n-1]^2}{r^2}\right)\tilde{v}_n, \tag{14}$$

$$\partial_t\hat{w}_n+\widehat{\mathbf{N}(\mathbf{u})}_{zn}=-\partial_z\hat{p}_n+\frac{1}{\mathrm{Re}}\left(\nabla_{rz}^2-\frac{n^2}{r^2}\right)\hat{w}_n, \tag{15}$$

where $\widetilde{N(u)}_{rn}=\widehat{N(u)}_{rn}+i\widehat{N(u)}_{\theta n}$ and $\widetilde{N(u)}_{\theta n}=\widehat{N(u)}_{rn}-i\widehat{N(u)}_{\theta n}$, with $\widehat{N(u)}_{zn}$, etc., representing the corresponding n component of the transformed nonlinear terms.

The appropriate boundary conditions to be applied at the axis ($r=0$) for this kind of modal decomposition of the velocity filed was described by Lopez *et al.*[25] and lead to

$$r=0:\quad\begin{cases}n=0: & \tilde{u}_o=\tilde{v}_o=\partial_r\hat{w}_o=\partial_r\hat{p}_o=0;\\ n=1: & \tilde{u}_1=\partial_r\tilde{v}_1=\hat{w}_1=\hat{p}_1=0;\\ n>1: & \tilde{u}_n=\tilde{v}_n=\hat{w}_n=\hat{p}_n=0.\end{cases} \tag{16}$$

The required boundary conditions for the pressure modes at the physical boundaries (inlet, outlet and pipe wall) are obtained by projecting the momentum equations onto the normal direction $\mathbf{n}$ of the domain. For the computation of the time evolution, a mixed implicit-explicit second order projection scheme based on backwards differentiation is employed.[25]

The spatial discretization employs Fourier expansion in the azimuthal direction. The infinite set of Fourier modes (8) is truncated at some finite wave number n_θ:

$$\mathbf{u}(z,r,\theta,t)=\sum_{n=-n_\theta}^{n_\theta-1}\hat{\mathbf{u}}_n(z,r,t)\exp(in\theta). \tag{17}$$

Since the modes have the symmetry property $\hat{\mathbf{u}}_{-n}=\hat{\mathbf{u}}_{+n}^*$, where the asterisk superscript denote the complex conjugate, in practice we need keep only the positive wave number half of the spectrum ($n\geq 0$). Spatial discretization in the meridianal (z,r) semiplane employs n_r Chebyshev spectral collocation points in r, and second-order, central finite-differences in z, with n_z points in the axial direction. This approach allow us to use the matrix diagonalization method,[26] whose computational complexity is of order $n_r\times n_z\times\min(n_r,n_z)$, to solve the three Helmholtz-type equations resulting from the momentum equations and the Poisson equation needed to get the pressure corrections. The nonlinear terms are evaluated using a pseudospectral method.[27]

Note that the spectral resolution in both the radial and azimuthal directions allow us to use a much less number of grid points in those directions than in the axial one, that is discretized by finite-differences. Therefore, for the geometrical configuration selected, $R_o=4$ and $z_f=60$, we have carried out the numerical simulations in a grid with $n_r=30$, $n_z=401$ and $n_\theta=8$ for the cases with $\mathrm{Re}=100$ and $\mathrm{Re}=250$, while more axial points were required ($n_z=501$) in those cases with the largest Reynolds number considered here, $\mathrm{Re}=400$. Several convergence tests conducted in finer grids (with $n_r=41$ radial points and $n_\theta=12$ azimuthal modes) suggested that this resolution level yield accurate results. The time step employed in the simulations was $\Delta t=0.02$, since no significant differences in the temporal evolution of the flow were found by using smaller time steps. In addition, to check out that the 3D structures found in this work were not affected by the particular length of the computational pipe used in the simulations, nor by the boundary conditions imposed at the pipe outlet, the 3D results with the largest values of both Re and S were reproduced by using a longer pipe with $z_f=80$.

IV. NUMERICAL RESULTS

A. Axisymmetric results

The 3D numerical code allow us to carry out axisymmetric simulations as well by just taking $n_\theta=0$ in the spectral representation (17). In the considered pipe geometry with $R_o=4$ and $z_f=60$, we have analyzed first the case of a jet-like velocity profile with $a=0.5$ in Eq. (8). The axisymmetric time evolution of the initial columnar flow shows that, for $100\leq\mathrm{Re}\leq 400$, the flow evolves towards a steady state solution of the axisymmetric Navier-Stokes equations that presents a region of reversed flow (a recirculating "bubble") if the relative swirl is high enough. This can be quantified by using the minimum axial velocity of the steady axisymmetric solution in the pipe domain as the control parameter, defined as

$$w_{\min}=\min[w(r,z)]_{0\leq r\leq R_o,0\leq z\leq z_f}. \tag{18}$$

Figure 1 represents $w_{\min}$ as a function of the swirl parameter S for $\mathrm{Re}=400$. It is observed that, as S increases,

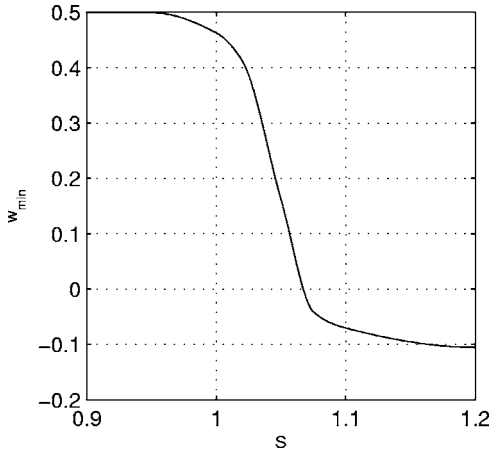

FIG. 1. $w_{\min}$ as a function of the swirl parameter S for Re=400 and $a=0.5$.

$w_{\min}$ decreases bellow its initial value 0.5 (which corresponds to the initial axial velocity far away from the axis). For S larger than a critical value, $S>S^*$, which for Re=400 is approximately $S^*=1.075$, the solution shows the presence of reversed flow, $w_{\min}<0$, indicating the occurrence of axisymmetric vortex breakdown in the fluid domain. To illustrate the structure of the flow with $w_{\min}<0$ for different Reynolds numbers, we have plotted in Fig. 2 contour lines of the axial velocity of the steady axisymmetric solution for a given swirl larger than S^*, $S=1.2$, and three different Reynolds numbers: 100, 250, and 400. These contours lines are in a meridianal plane (y,z), with $y=r$ for $\theta=0$ and $y=-r$ for $\theta=\pi$. It should be pointed out that we have used axial velocity contours to visualize the structure of the flow, instead of the more usual streamlines in axisymmetric flows,

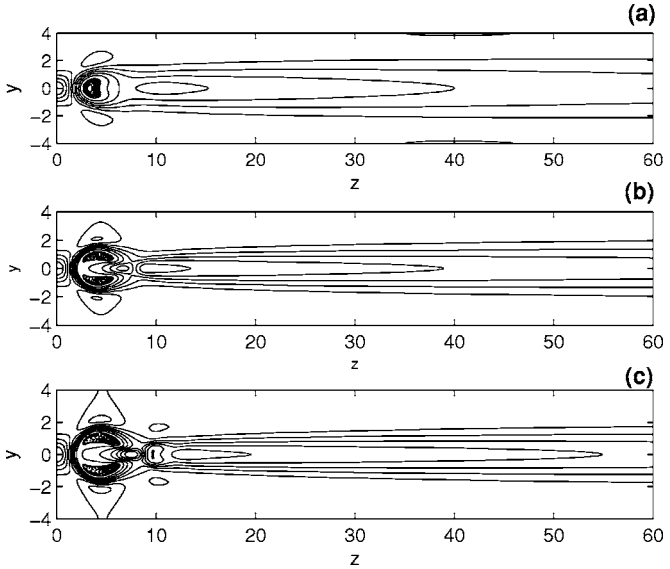

FIG. 2. Contours of the axial velocity component, w, in the (z,y) plane corresponding to the steady axisymmetric solution of the N-S equations with $a=0.5$ and $S=1.2$ for three different Reynolds numbers: (a) Re=100, (b) Re=250 and (c) Re=400. Ten positive and ten negative equidistant contours of w are plotted in the following intervals: between its minimum value and zero (dashed lines) and between zero and its maximum value (continuous lines).

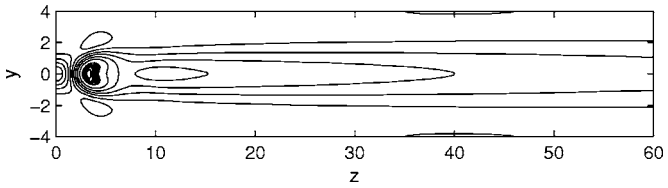

FIG. 3. Contours of the axial velocity component, w, in the (z,y) plane corresponding to the steady axisymmetric solution of the N-S equations with $a=0.5$, $S=1.1$, and Re=250. Ten positive and ten negative equidistant contours of w are plotted in the following intervals: between its minimum value and zero (dashed lines) and between zero and its maximum value (continuous lines).

because we want to compare these axisymmetric results with the 3D simulations of the next section. In the three cases plotted, a steady "bubble" of recirculating flow (dotted lines represents negative values of the axial velocity) is formed close to the pipe entrance. The flow upstream that region (where $w>0$) does not change too much when the Reynolds number is increased. However, the bubble size increases both in the radial and in the axial directions as the Reynolds number increases, and even a new small bubble is observed downstream of the first one (near $z\simeq 10$) for Re=400.

Since the three axisymmetric solutions depicted in Fig. 2 will be used as initial conditions for the 3D simulations reported below, and as the basic flows in the stability analysis of Sec. V, to study the influence of Re on the appearance of 3D instabilities, we will name them as follows:

Case I: $a=0.5$, $S=1.2$, Re=100 [Fig. 2(a)];

Case II: $a=0.5$, $S=1.2$, Re=250 [Fig. 2(b)];

Case III: $a=0.5$, $S=1.2$, Re=400 [Fig. 2(c)].

Another case which we shall consider in the 3D numerical simulations of Sec. IV B, but now starting the 3D computations from the original columnar vortex (8), to compare the 3D results with the axisymmetric time evolution, will be

Case IV: $a=0.5$, $S=1.1$, Re=250 (Fig. 3).

This case corresponds to a value of the swirl parameter larger than S^* [$S=1.1>S^*(\mathrm{Re}=250,a=0.5)$], but closer to S^* than in case II. The contour lines of the axial velocity corresponding to the axisymmetric steady state solution are depicted in Fig. 3 [compare with Fig. 2(b)].

Finally, we have also analyzed in this section the dependence on the swirl parameter of the behavior of columnar flows given by (8) for the case of a wake-like velocity profile with $a=1.5$. The axisymmetric time evolution of these columnar flows shows that, for a fixed Reynolds number (say, Re=250), the flow evolves towards a steady state solution of the Navier-Stokes equations that again presents reverse flow if the swirl is sufficiently large (see Fig. 4). Note that the swirl parameter for axisymmetric vortex breakdown is significantly larger now ($S^*\simeq 1.85$) than for the case considered

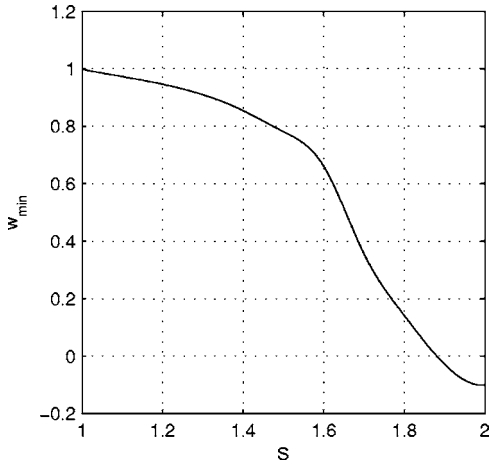

FIG. 4. w_{min} as a function of the swirl parameter S for Re=250 and $a=1.5$.

above of a jet-like initial velocity profile with $a=0.5$. We have plotted in Fig. 5 the contour lines of the axial velocity for the axisymmetric steady solution corresponding to

Case V: $a=1.5$, $S=2$, Re=250 (Fig. 5),

which will be also used as an initial condition in the 3D simulations described in the next section.

B. 3D results and discussion

Here we present the results of the 3D numerical simulations for the five cases considered in the above axisymmetric numerical simulations. With the first three cases we investigate the role of viscosity on the subsequent 3D evolution of the flow starting from the axisymmetric steady state with the "bubble" of recirculating flow. With the fourth case we start the numerical simulation from the initial columnar flow to show that the nonaxisymmetric flow, i.e., the spiral or helicoidal form vortex breakdown, is formed sufficiently after the axisymmetric bubble form of vortex breakdown has developed. With this case we also account for the effect of the swirl parameter on the helical breakdown. Finally, the fifth case will show the differences between the evolution of a vortex with a wake-like axial velocity profile at the entrance and a vortex with a jet-like form at the inlet.

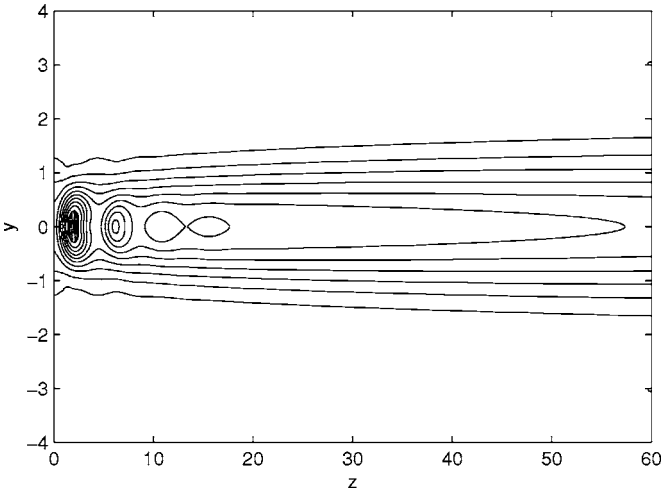

FIG. 5. Contours of the axial velocity component, w, in the (z,y) plane corresponding to the steady axisymmetric solution of the N-S equations with $a=1.5$, $S=2$ and Re=250. Ten positive and ten negative equidistant contours of w are plotted in the following intervals: between its minimum value and zero (dashed lines) and between zero and its maximum value (continuous lines).

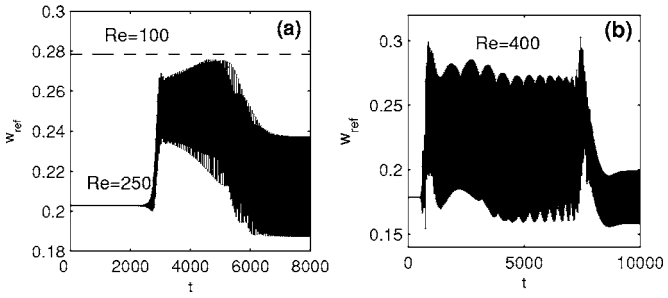

FIG. 6. Temporal evolution of the axial velocity w_{ref} at a given position $\mathbf{x}_{ref}=[r=0.4,\theta=0,z=30]$ for a flow with $S=1.2$, $a=0.5$, and three different Reynolds numbers: Re=100 (case I) and Re=250 (case II) (a); and Re=400 (case III) (b).

Figures 6(a) and 6(b) depict the time evolution of the axial velocity w_{ref} at a given position $\mathbf{x}_{ref}=[r=0.4,\theta=0,z=30]$ behind the axisymmetric bubble of recirculating flow for the cases I, II, and III. It can be seen in Fig. 6(a) that, for Re=100, the reference velocity does not change with time (dashed line), indicating that the initial axisymmetric steady solution remains stable during the 3D numerical simulation. However, for larger values of the Reynolds number, Fig. 6 shows that, after a certain period of time, which becomes shorter as the Reynolds number increases, w_{ref} begins to change in time, indicating that the flow becomes unsteady and nonaxisymmetric. A closer look at the time evolution of cases II and III for the largest instants of time considered (Fig. 7) shows that the flow becomes purely periodic at the end, with a frequency $\omega_{3D}\sim 0.43$ for Re=250, and slightly higher, $\omega_{3D}\sim 0.44$, for Re=400. The reason for this behavior is the development of nonaxisymmetric instabilities in the flow in both cases (II and III), giving rise to an unsteady nonaxisymmetric flow which, after a relatively long transient period, finishes up with a simple wave-like behavior. In order to illustrate this, we have plotted in Fig. 8 the temporal evo-

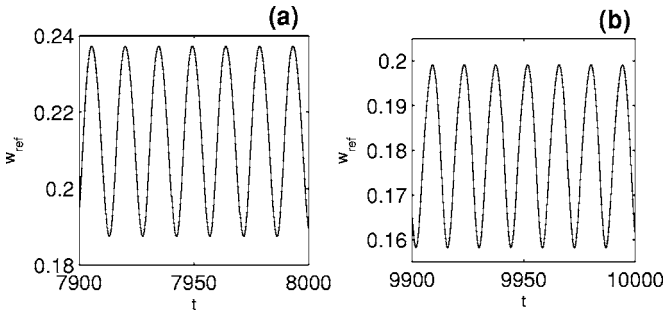

FIG. 7. Detail of the large time behavior of w_{ref} for: case II (a) with $\omega_{3D}\sim 0.43$, and case III (b) with $\omega_{3D}\sim 0.44$.

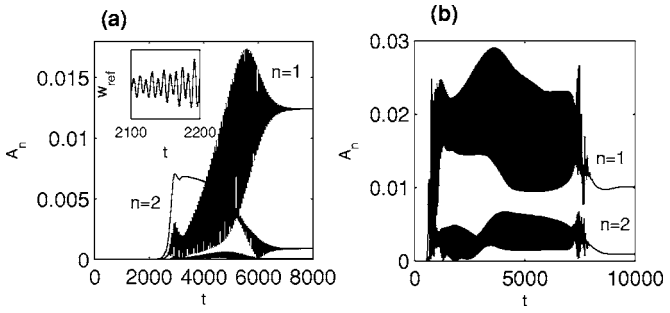

FIG. 8. Temporal evolution of the different amplitudes A_n [defined in Eq. (19)] for different nonaxisymmetric modes $n>0$ corresponding to case II (a) and case III (b). The inset in (a) is shown to compute the frequency of the mode $n=2$ at its initial stages of development.

lution of the amplitudes of the different nonaxisymmetric modes for the axial velocity in the modal decomposition (17) at the same location $\mathbf{x}_{\mathrm{ref}}$,

$$A_n(t) \equiv |\hat{w}_n(r_{\mathrm{ref}}, z_{\mathrm{ref}}, t)|, \quad n > 0. \tag{19}$$

For Re=250 [Fig. 8(a)], A_2 is the first mode that becomes destabilized, increasing very fast in time, while the amplitudes of the other modes begin to increase later and more slowly. Eventually, for a sufficiently large time, the amplitude A_2 decays, and the mode corresponding to A_1 becomes the dominant one at the final state (the amplitude A_3 and those corresponding to higher modes not shown in the figure remain always very small). For Re=400, Fig. 8(b) shows that the nonaxisymmetric perturbations develop appreciably faster than for Re=250. In addition, the time required for the amplitudes of the nonaxisymmetric modes to reach the final purely oscillatory state is much larger. Another significant difference in this case is that the amplitude A_1 is appreciably larger that A_2 from the beginning of the 3D instability, and remains so until the final state.

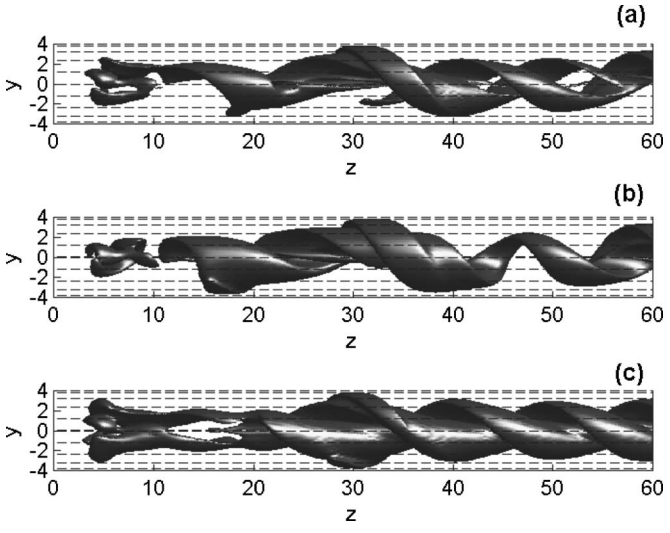

FIG. 9. Three-dimensional perspectives of the perturbations of the circulation corresponding to case II at time $t=4800$. (a) Isosurface of Γ_p, (b) isosurface of the $|n|=1$ component, and (c) isosurface of the $|n|=2$ component. All the isosurfaces are chosen at 10% of their maximum values.

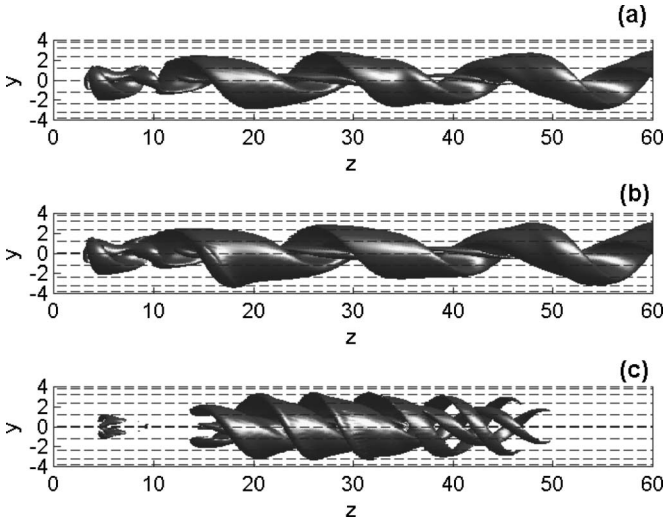

FIG. 10. As in Fig. 9, but for $t=8000$.

The above results suggest that, in case II (Re=250), the flow first develops a double helicoidal structure behind the bubble (the mode $n=2$ is the dominant one at the beginning of the 3D instability), evolving later towards a nearly single helicoidal structure ($n=1$). However, in case III (Re=400), the mode $n=1$ seems to be the dominant one from the beginning of the instability, but with a significant contribution of the mode $n=2$ remaining. In order to corroborate this picture, we have plotted in Figs. 9–11 several isosurfaces of the circulation $\Gamma=rv$ at different instants of time. In particular, we have used the modal decomposition (17) to express the circulation as the sum of an axisymmetric main part and a nonaxisymmetric perturbation,

$$\Gamma(r,\theta,z,t) = \hat{\Gamma}_o(r,z,t) + \sum_{n\neq 0} \hat{\Gamma}_n(r,z,t)\exp(in\theta)$$

$$\equiv \Gamma_{\mathrm{main}}(r,z,t) + \Gamma_p(r,\theta,z,t). \tag{20}$$

Figure 9 shows three-dimensional perspectives of the perturbation Γ_p of the circulation for case II at the time $t=4800$

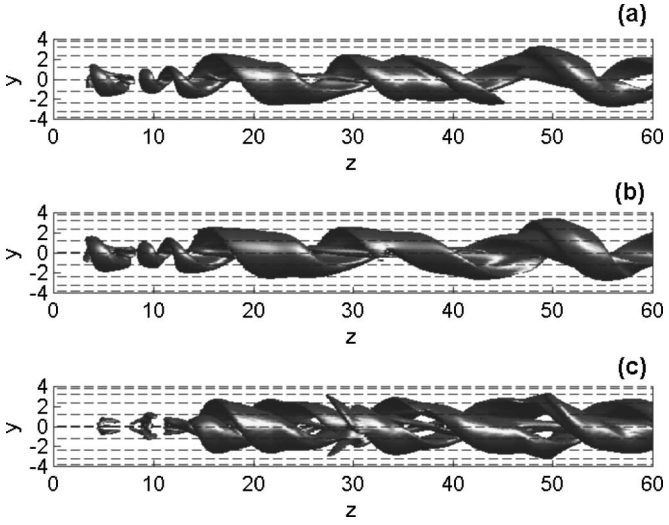

FIG. 11. As in Fig. 9, but for case III at $t=7000$.

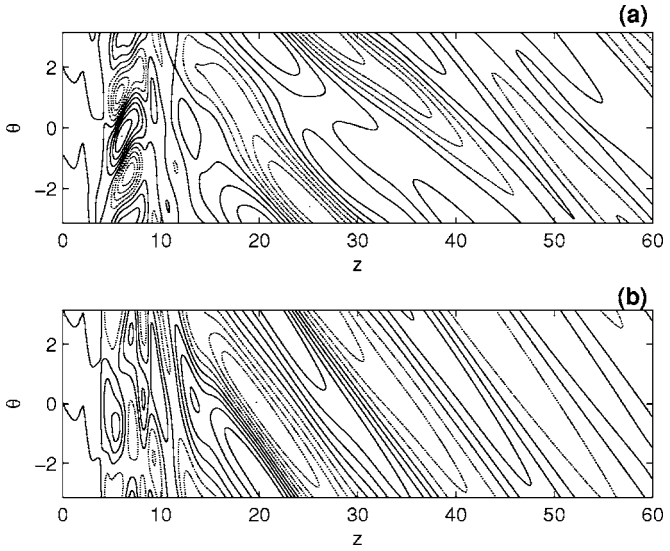

FIG. 12. Contour lines of Γ_p on the (θ,z) plane for $r=r_{\mathrm{ref}}=0.4$ and for two different instants of time [(a) $t=4900$ and (b) $t=8000$] for case II. Five positive and five negative equidistant contours of Γ_p are plotted in the following intervals: between its minimum value and zero (dashed lines) and between zero and its maximum value (continuous lines).

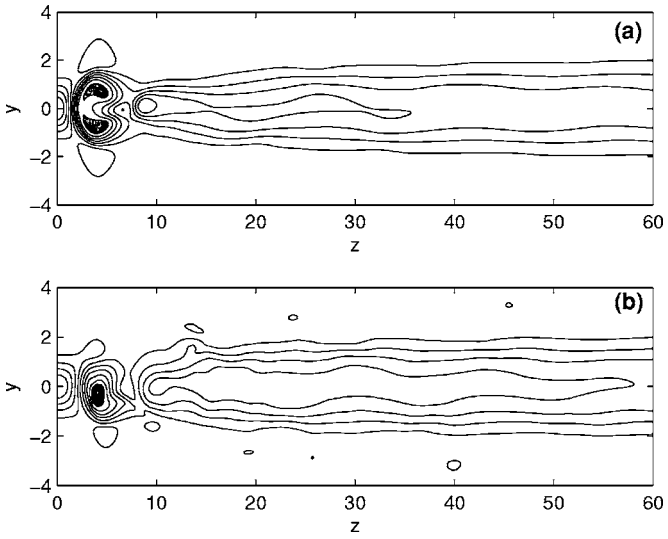

FIG. 14. Contour lines of the axial velocity component, w, on the (z,y) plane of the 3D solution for: (a) case II at $t=8000$, and (b) case III at $t=10000$. Ten positive and ten negative equidistant contours of w are plotted in the following intervals: between its minimum value and zero (dashed lines) and between zero and its maximum value (continuous lines).

for which, according to Fig. 8(a), both modes $|n|=1$ and $|n|=2$ are present in the flow at approximately the same level. Figure 9(a) displays an isosurface of the whole perturbation Γ_p corresponding to the 10% of its maximum value, while Figs. 9(b) and 9(c) display the isosurfaces for its $|n|=1$ and $|n|=2$ components, respectively (both corresponding to the 10% of their respective maximum values). The double-helicoidal structure of the flow is clear in Fig. 9(a), but it is distorted in relation to the pure mode $|n|=2$, depicted in Fig. 9(c), due to the relative importance of the component $|n|=1$ [Fig. 9(b)]. For subsequent times, the relative importance of the mode $|n|=2$ decays and, for $t=8000$ (Fig. 10), the downstream flow corresponds to an almost single helical structure [note that Figs. 10(a) and 10(b) are practically coincident].

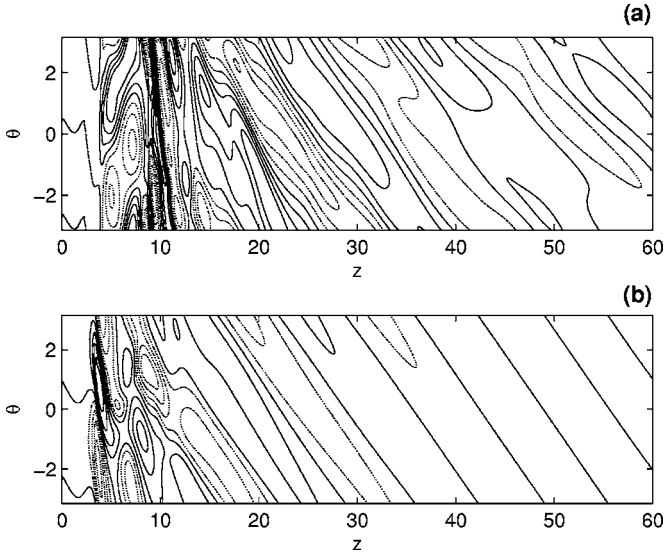

FIG. 13. As in Fig. 12, but for case III at $t=7000$ (a), and at $t=10000$ (b).

Figure 11 shows three-dimensional perspectives of the perturbation of the circulation for case III (Re=400) at $t=7000$. The structure of the flow [Fig. 11(a)] is a mixing of the mode $|n|=1$ [Fig. 11(b)] and the mode $|n|=2$ [Fig. 11(c)]. However, for larger times, the situation is similar to case II, becoming the mode $|n|=1$ the dominant one.

To find out the winding direction of the helicoidal, or the double helicoidal, vortex breakdown structures appearing in the wake of the axisymmetric breakdown bubble during the temporal evolution of the flow, one may use the contour lines of the nonaxisymmetric part of the circulation Γ_p in a plane (θ,z) for some value of r at several instants of time. Figure 12 shows these contour lines at $r=r_{\mathrm{ref}}=0.4$ for case II (Re =250) at $t=4900$ and at $t=8000$. For $t=4900$ [Fig. 12(a)], the inclination of the contour lines in the region $5<z<10$ (approximately) indicates negative values of the azimuthal wave numbers, while the change in the inclination of the contours in the main downstream region $10<z<60$ indicates positive values of n. However, for $t=8000$ [Fig. 12(b)], almost all the

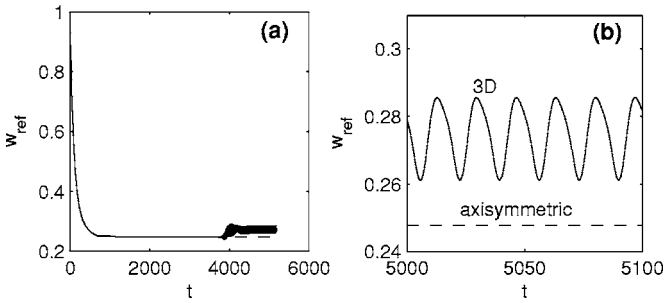

FIG. 15. Comparison between the time evolution of the axial velocity, w_{ref}, at the fixed position $\mathbf{x}_{\mathrm{ref}}$, obtained from the 3D numerical simulation (solid line) and from the axisymmetric one (dashed line) for case IV. Part (a) shows the whole evolution from the initial columnar flow, and part (b) the periodic character of the resulting 3D flow at the final stages with $\omega_{3D}\sim 0.37$.

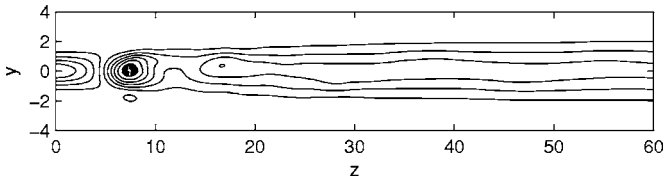

FIG. 16. Contour lines of the axial velocity component, w, on the (z,y) plane of the 3D solution for case IV at $t=5200$. Ten positive and ten negative equidistant contours of w are plotted in the following intervals: between its minimum value and zero (dashed lines) and between zero and its maximum value (continuous lines).

contour lines have the same (positive) slope, $n>0$. These results suggest that several types of nonaxisymmetric instabilities develop in the flow (both with $n>0$ and with $n<0$), but only the perturbations with $n>0$ remain for sufficiently large times. Figure 13 shows the contour lines of Γ_p in the (θ,z) plane at $r=r_{\mathrm{ref}}=0.4$ for case III (Re=400) at $t=7000$ and at $t=10000$. The situation in this case is quite similar to that observed for Re=250: waves with $n>0$ and $n<0$ develop in the flow, but only the $n>0$ ones, particularly with $n=+1$, survive at later times.

To finish with this long discussion of the results for the cases II and III, we have plotted in Fig. 14 contour lines of the axial velocity in a meridianal plane (y,z) for $\theta=0$ (and $\theta=\pi$ if $y<0$) at $t=8000$ (case II), and at $t=10000$ (case III). By comparing with the axisymmetric contour lines of Figs. 2(b) and 2(c), respectively, it is clear that, case II, the flow remains mostly unaffected inside the recirculating bubble and in the region upstream of it; however, 3D effects are clearly visible in the wake behind the bubble, with a loss of symmetry with respect to the line $y=0$ (axis). For case III, 3D effects are more pronounced, and one observes important differences between the 3D flow and the axisymmetric initial one even inside and upstream the breakdown bubble [compare Figs. 2(c) and 14(b)].

Let us now present the 3D results for case IV. As mentioned above, we have started the 3D simulation in this case directly from the columnar vortex (8) in order to give support to the hypothesis that the development of the helicoidal vortex breakdown necessarily requires the appearance first of a region of reverse flow (breakdown bubble). In addition, we have selected in this case a different (smaller) value of swirl parameter ($S=1.1$) in order to study the influence of this parameter on the temporal development of the nonaxisymmetric perturbations. Figure 15 shows the comparison between the time evolution of the axial velocity, w_{ref}, at the fixed position $\mathbf{x}_{\mathrm{ref}}=[r=0.4,z=30,\theta=0]$, obtained from the 3D numerical simulation (solid line) and from the axisymmetric one (dashed line). It is observed in Fig. 15(a) that in

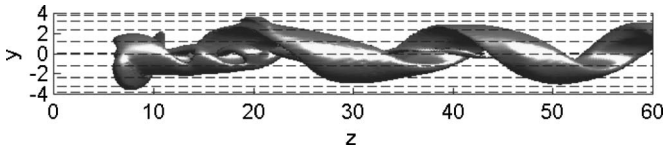

FIG. 17. Three-dimensional perspectives of Γ_p corresponding to case IV at $t=5200$. The isosurface of Γ_p is chosen at 10% of its maximum value.

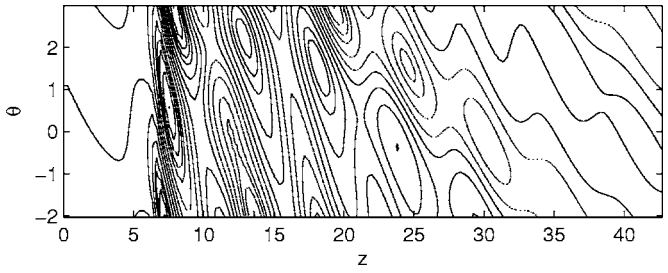

FIG. 18. Contour lines of Γ_p on the (θ,z) plane for $r=r_{\mathrm{ref}}=0.4$ at $t=5200$ for case IV. Five positive and five negative equidistant contours of Γ_p are plotted in the following intervals: between its minimum value and zero (dashed lines) and between zero and its maximum value (continuous lines).

both simulations w_{ref} tends to a steady value which corresponds to the axisymmetric steady solution with reverse flow represented in Fig. 3. However, some time after this axisymmetric solution is reached, nonaxisymmetric instabilities develop in the flow that evolve towards a periodic nonaxisymmetric flow. The 3D character of the resulting final flow is shown in Fig. 16, which displays contour lines of the axial velocity at $t=5200$ on the meridianal plane $\theta=0$. The frequency of the oscillations, $\omega_{3\mathrm{D}}\simeq 0.37$ [see Fig. 15(b)], is smaller than the frequency of the oscillation observed in case II for the same Re ($\omega_{3\mathrm{D}}\simeq 0.42$), indicating that the frequency of the oscillations increases with the swirl of the initial flow. The helicoidal ($|n|=1$) structure of the 3D flow can be seen in Fig. 17, which displays an isosurface of Γ_p corresponding to 10% of its maximum value at $t=5200$. Finally, the contour lines of Γ_p on the (θ,z) plane, shown in Fig. 18 for $r=r_{\mathrm{ref}}=0.4$ at $t=5200$, indicate that the resulting helicoidal wave corresponds to $n>0$.

To end this section we present the 3D results for case V, which we have selected to analyze the influence of the inlet *axial* velocity profile in the development of the 3D flow. Figure 19 shows the time evolution of the axial velocity w_{ref} at the fixed position $\mathbf{x}_{\mathrm{ref}}=[r=0.4,z=30,\theta=0]$. The initial axisymmetric flow evolves, after a transient, towards a periodic 3D flow with a relatively large frequency $\omega_{3\mathrm{D}}\sim 1.4$ [see Fig. 19(b)]. As pointed out above, our computations show that the frequency of the final wake behind the bubble increases with the swirl strength of the initial flow: $\omega_{3\mathrm{D}}\sim 0.43-0.44$ for cases II and III with $S=1.2$, $\omega_{3\mathrm{D}}\sim 0.37$ for case IV with $S=1.1$, and now $\omega_{3\mathrm{D}}\sim 1.4$ for case V with $S=2$ (see Fig. 20).

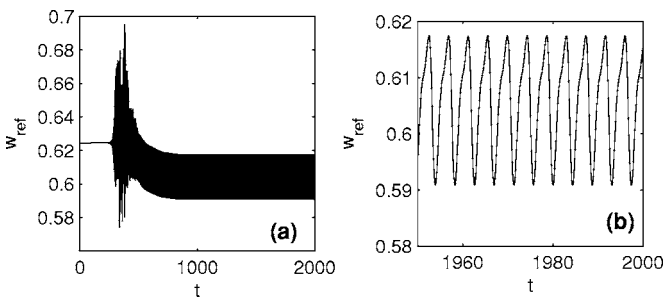

FIG. 19. Time evolution of the axial velocity, w_{ref}, at the fixed position $\mathbf{x}_{\mathrm{ref}}$, obtained from the 3D numerical simulation for case V. Part (a) shows the whole evolution from the axisymmetric steady flow, and part (b) the periodic character of the resulting 3D flow with $\omega_{3\mathrm{D}}\sim 1.4$.

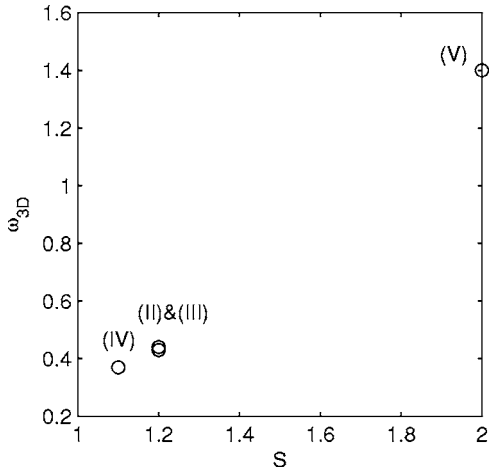

FIG. 20. Numerical frequency ω_{3D} as a function of S for Re=250. The circles correspond to the frequencies obtained in the 3D numerical simulations for the cases indicates in the figure.

The 3D character of the resulting flow is shown in Fig. 21, that displays contour lines of the axial velocity at $t=2000$. It may be noted the large differences between the resulting 3D flow and the initial axisymmetric flow (Fig. 5). In particular, the region of reverse flow completely disappear during the 3D evolution (there is no negative axial velocity in the whole domain). This result is qualitatively different from the results obtained for cases II, III, and IV with a jet-like velocity profile at the inlet, for which the 3D evolution always preserves (though distorted) the bubble of reverse flow near the entrance of the pipe. Following with the presentation of the results for case V, the helicoidal structure of the flow can be seen in Fig. 22, that displays the isosurfaces of Γ_p [Fig. 22(a)], and its components for the modes $|n|=1$ [Fig. 22(b)], and $|n|=2$ [Fig. 22(c)], all of them corresponding to the 10% of their respective maximum values at $t=2000$. The resulting wake flow presents a superposition of helicoidal and double-helicoidal waves, but with a single helical flow ($|n|=1$) exiting the pipe. The maximum amplitude ratio between modes $|n|=2$ and $|n|=1$ is just 0.00596. Finally, the contour lines of Γ_p in the (θ,z) plane, shown in Fig. 23 for $r=r_{\mathrm{ref}}=0.4$ at $t=2000$, indicates that $n>0$ $(n=+1)$.

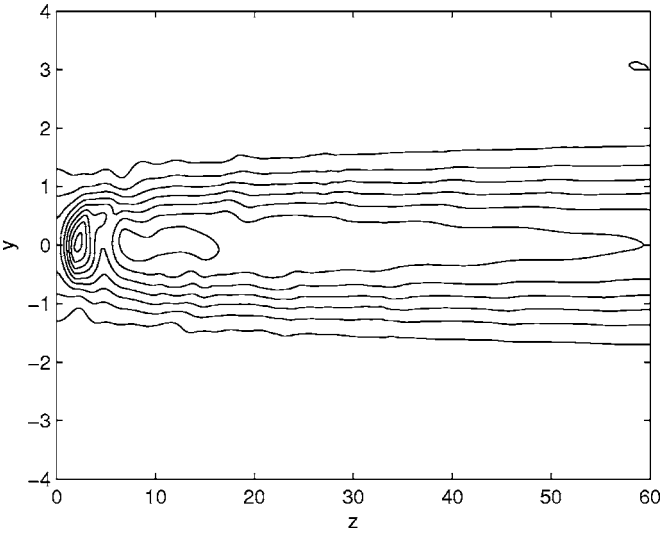

FIG. 21. Contour lines of the axial velocity component, w, on the (z,y) plane of the 3D solution for case V at $t=5200$. Ten positive equidistant contours of w are plotted in the interval between zero and its maximum value (no recirculating flow remains).

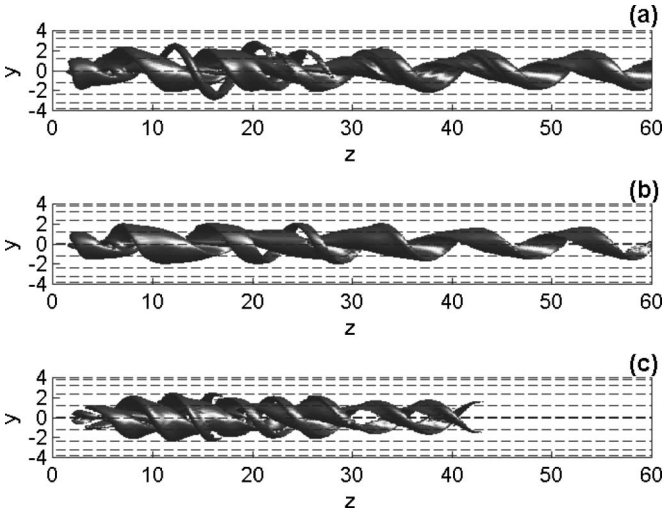

FIG. 22. Three-dimensional perspectives of the perturbations of the circulation corresponding to case V at $t=2000$. (a) Isosurface of Γ_p, (b) isosurface of the mode with $|n|=1$, and (c) isosurface of the mode with $|n|=2$. All the isosurfaces are chosen at 10% of their maximum values.

V. LOCAL STABILITY ANALYSIS

A. Formulation of the problem

The full Navier-Stokes numerical simulations of the previous section strongly suggest that the helical vortex breakdown structures develop only after a recirculating axisymmetric bubble has been formed in the transient evolution of the flow. Following the ideas of Pier and Huerre,[17,18] who have recently shown that the self-sustained nonlinear oscillating frequency of wake-like velocity profiles can be determined by the absolute frequency of the local stability analysis, we have performed here a linear absolute-convective analysis of those axisymmetric flows which presents a recirculating bubble. By means of a simple linear, spatial stability analysis carried out in the sections of the pipe where the intermediate axisymmetric flow presents reverse flow (nega-

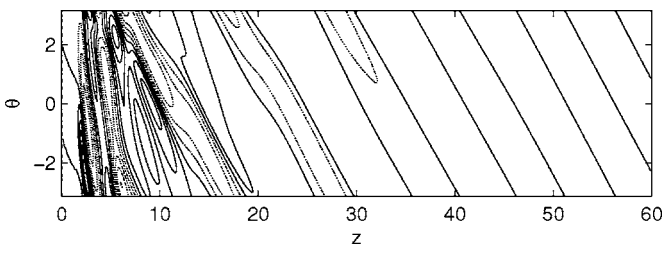

FIG. 23. Contour lines of Γ_p on the (θ,z) plane for $r=r_{\mathrm{ref}}=0.4$ for case V at $t=2000$. Five positive and five negative equidistant contours of Γ_p are plotted in the following intervals: between its minimum value and zero (dashed lines) and between zero and its maximum value (continuous lines).

tive axial velocity at the axis), we have tried to identify the frequencies and the dominant azimuthal wave numbers observed in the 3D simulations.

We first proceed to decompose both the velocity and pressure fields in a basic part, $\mathbf{U_o}=(U_o,V_o,W_o)$ and P_o, and a perturbation, $\mathbf{u}'=(u',v',w')$ and p',

$$u=U_o+u', \quad v=V_o+v', \quad w=W_o+w', \quad p=P_o+p', \tag{21}$$

where the basic flow corresponds to any of the previously computed axisymmetric steady solutions of the N-S equations considered above (cases I–V), all of them with a region of reverse flow. Taking into account that in our simulations $\mathrm{Re}\gg 1$, we use the method of multiple scales by introducing a *slow* axial variable $Z=z/\mathrm{Re}$, and by expressing the unsteady perturbations in terms of a slowly varying amplitude and axial wave number in the form

$$\{\mathbf{u}',p'\}(z,r,\theta,t)=\sum_n \{\mathbf{u_n},p_n\}(Z,r) \times\exp\left(\mathrm{Re}\int^Z k_n(\xi)d\xi+in\theta-i\omega t\right). \tag{22}$$

In this expression, n is the azimuthal wave number, while $\omega\equiv\Omega\delta/w_c$ and $k_n\equiv\delta K_n$ are the nondimensional frequency and axial wave numbers, respectively, being Ω and K_n the corresponding dimensional values. We will perform a spatial stability analysis, where ω is real and the k_n are complex numbers. The real and the imaginary parts, γ and α, of the complex axial wave number,

$$k_n\equiv\gamma_n+i\alpha_n, \tag{23}$$

are the exponential growth rate and the axial wave number, respectively, for each n.

Introducing (22) into the Navier-Stokes equations (1)–(4), retaining only linear terms of the perturbations, neglecting terms of order $(1/\mathrm{Re})^2$ and the nonparallel terms arising from the axial variation of both the basic and perturbated flows, one arrives at the following set of linear equations for the amplitude of the perturbations:

$$w_nk_n+\frac{\partial u_n}{\partial r}+\frac{u_n}{r}+\frac{inv_n}{r}=0, \tag{24}$$

$$i\omega u_n-k_nW_ou_n-U_o\frac{\partial u_n}{\partial r}-u_n\frac{\partial U_o}{\partial r}-\frac{\partial p_n}{\partial r} +\frac{1}{\mathrm{Re}}\left[\frac{\partial^2u_n}{\partial r^2}+\frac{1}{r}\frac{\partial u_n}{\partial r}+\left(k_n^2-\frac{n^2}{r^2}\right)u_n-\frac{u_n}{r^2}-2in\frac{v_n}{r^2}\right]=0, \tag{25}$$

$$i\omega v_n-k_nW_ov_n-U_o\frac{\partial v_n}{\partial r}-U_o\frac{v_n}{r}-in\frac{p_n}{r} +\frac{1}{\mathrm{Re}}\left[\frac{\partial^2v_n}{\partial r^2}+\frac{1}{r}\frac{\partial v_n}{\partial r}+\left(k_n^2-\frac{n^2}{r^2}\right)v_n+2in\frac{u_n}{r^2}-\frac{v_n}{r^2}\right]=0, \tag{26}$$

$$i\omega w_n-k_nW_ow_n-U_o\frac{\partial w_n}{\partial r}-u_n\frac{\partial W_o}{\partial r}-k_np_n +\frac{1}{\mathrm{Re}}\left[\frac{\partial^2w_n}{\partial r^2}+\frac{1}{r}\frac{\partial w_n}{\partial r}+\left(k_n^2-\frac{n^2}{r^2}\right)w_n\right]=0. \tag{27}$$

By neglecting the nonparallel terms (near-parallel approximation), the global stability problem is reduced to a local stability analysis to be solve at different z stations.

The system have been solved subjected to the following radial boundary conditions for each azimuthal wave number n:

$$\text{at } r=R_o, \quad u_n=v_n=\partial_rw_n=0; \tag{28}$$

$$\text{at } r=0, \quad \begin{cases} u_n=v_n=0, \quad \partial_rw_n=0 & (n=0),\\ u_n\pm iv_n=0, \quad \partial_ru_n=0, \quad w_n=0 & (n=\pm1),\\ u_n=v_n=w_n=0 & (|n|>1). \end{cases} \tag{29}$$

Note that it is assumed that the perturbations do not modify the basic flow at the pipe wall $r=R_o$, and satisfy the same boundary condition as the basic flow at the axis. Observe, however, that the stability equations are not symmetric with respect to n (since the basic swirl velocity v_o is not zero), and therefore both positive and negative azimuthal wave numbers n have to be considered.

B. Numerical scheme

It proves convenient to rewrite Eqs. (24)–(27) in the form

$$0=\left[\mathbf{L_1}+k_n\mathbf{L_2}+\frac{k_n^2}{\mathrm{Re}}\mathbf{L_3}\right]\cdot\mathbf{S}, \tag{30}$$

where $\mathbf{L_1}$, $\mathbf{L_2}$, and $\mathbf{L_3}$ are complex matrices which depend on z (only through the basic flow) and r, and $\mathbf{S}\equiv\{\mathbf{u}_n,p_n\}$. To solve (30) numerically, the equations are discretized in the r direction using the same Chebyshev spectral collocation technique employed in the full numerical simulations. The nonlinear (quadratic) eigenvalue problem (30) for k_n is solved using the linear companion matrix method described in Ref. 28. The resulting linear eigenvalue problem is numerically solved with the help of an eigenvalue solver subroutine DGVCCG from the IMSL library, which provides the entire spectrum of eigenvalues and eigenfunctions. Spurious eigenvalues were ruled out by comparing the computed spectrums obtained for different values of the number of collocation points n_r. For most of the computations reported below, values of n_r between 31 and 41 were enough to obtain the eigenvalues with at least 7 significant figures, as it was checked out for every result given below by using larger values of n_r.

C. Results

We have applied the above lineal stability analysis to the basic axisymmetric flows considered in the numerical simulations of Sec. IV A (cases I–V), all of them with a region of reverse flow close to the pipe inlet. Since the stability analy-

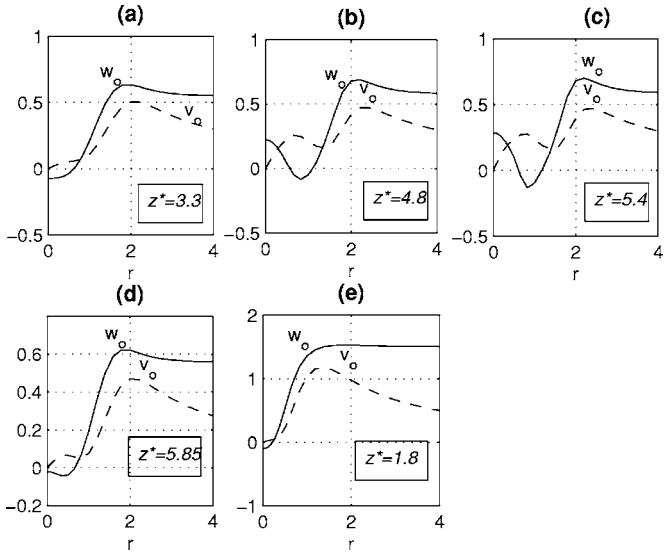

FIG. 24. Axial (continuous line) and azimuthal (dashed line) velocities profiles of the basic flow at the axial position $z=z^*$ where the local stability analysis is carried out, case I (a), case II (b), case III (c), case IV (d), and case V (e).

sis that we propose here is local, one important preliminary question is the selection of the axial station to perform the stability analysis in order to predict the main 3D features of the subsequent flow. We have seen in the 3D simulations of the previous section that the flow develops a helicoidal structure only after a region of reverse flow (axisymmetric breakdown bubble) is present in the domain. This fact suggests us the idea of carrying out the stability analysis at the z station where the axial velocity of the axisymmetric basic flow reaches its minimum (negative) value, that will be designed by z^*. Figure 24 shows the axial (solid lines) and azimuthal (dashed lines) velocity profiles of the basic axisymmetric flows corresponding to the five cases considered as functions of r at $z=z^*$ (the corresponding values of z^* are indicated in the respective figures; see also Figs. 2, 3, and 5). As we shall see, the local stability analysis applied to these velocity profiles predicts surprisingly well the existence and the properties of the subsequent 3D wake, provided that the flow is absolutely unstable. As a matter of fact, to apply the empirical frequency selection of Pierrehumbert,[19] one should examine the existence of absolute instabilities regions in the whole axisymmetric flow, particularly inside the bubble region of flow reverse, and look for the most (absolutely) unstable perturbation. But, as we show below, this most unstable perturbation is located at, or very close to, the axial station where the axial velocity presents its minimum (negative) value.

For a given azimuthal wave number n and for real frequencies ω (spatial stability analysis), we solve Eq. (30) to obtain the complete eigenvalue spectrum. Let us start with case I [velocity profiles at $z=z^*$ given in Fig. 24(a)]. Following the definitions of convective and absolute instabilities given by Huerre and Monkewitz,[29] we find that the flow is only convectively unstable for perturbations with $n=1$. This can be seen in Fig. 25, where we have plotted α and γ as functions of ω for the most unstable modes (largest growth rate γ) with $n=1$. Observe that α increases with ω [Fig. 25(a)], indicating that the group velocity is always positive, and that the growth rate is positive in a certain range of frequencies [Fig. 25(b)]. Therefore, the amplitude of any perturbation with $n=1$ and with a frequency in that range grows as z increases. In the full numerical simulations for this case performed in Sec. IV B we have not appreciated the spatial growth of any nonaxisymmetric perturbation. This can be due to the fact that the spatial growth rates are quite small, so that a much longer pipe would be necessary to appreciate the downstream amplification of just the numerical noise to visualize these convective instabilities (in the form of travelling waves) in that specific range of frequencies.

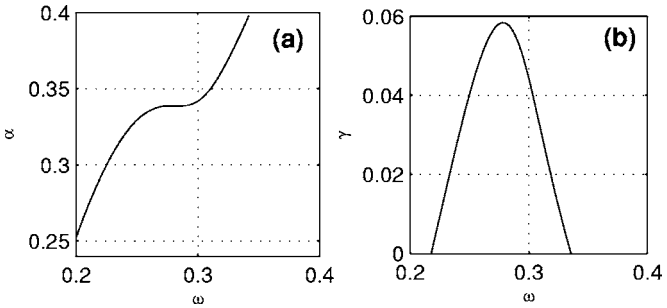

FIG. 25. $\alpha(\omega)$ (a) and $\gamma(\omega)$ (b) for the most unstable mode with $n=1$ corresponding to case I.

The situation is qualitatively different for the rest of the cases depicted in Figs. 24(b)–24(d) (cases II–V), where the velocity profiles are found to be not just convectively unstable, but also absolutely unstable. To find out these absolute instabilities one should look for the presence of saddle points in the dispersion relation, arising from the coalescence of two spatial branches located at opposite sides of the (α, γ) plane (Briggs-Bers criterion; see, e.g., Huerre and Monkewitz[29] and, for a more recent account, Chomaz[30]). By varying the imaginary part of the frequency, ω_i, we have found a number of such saddle points for the four cases considered and for different values of the azimuthal wave number n. The main results are compiled in Table I. There we show the critical values of the real part of the frequency, ω^*, the imaginary part of the frequency (absolute growth rate), ω_i^*, and the corresponding values of γ^* and α^* at which

TABLE I. Absolute instabilities: Characteristics of all the saddle points in the dispersion relations found in the different cases considered.

Case	n	ω^*	α^*	γ^*	ω_i^*
II	−1	0.242	1.6	0.6	−0.0245
II	+1	0.38	1.8	1.7	−0.128
II	+2	0.43	0.85	0.25	+0.021
III	−1	0.215	1.52	0.45	−0.0075
III	+1	0.435	0.5	3.3	+0.012
III	+2	0.4104	0.22	0.1	−0.0195
IV	+1	0.35	0.46	5.6	+0.0435
IV	+2	0.59	0.8	0.9	+0.009
V	−1	1.8	0.3	3.3	+0.16
V	+1	1.3	1.5	0.8	+0.31
V	+2	2.4	1.	1.5	−0.052

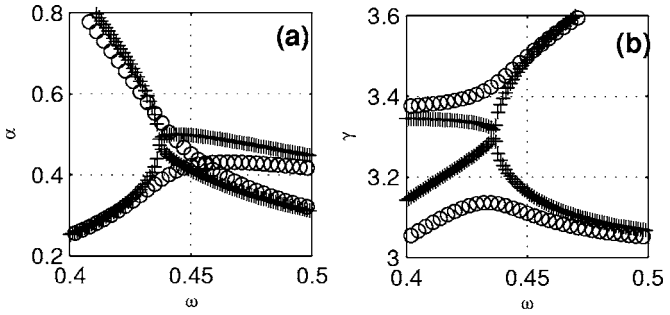

FIG. 26. $\alpha(\omega)$ (a) and $\gamma(\omega)$ (b) in the coalescence of two branches into a saddle point in the dispersion relation for case III with $n=1$. Lines marked with ○ corresponds to the spatial branches ($\omega_i=0$), which merge into a saddle point for $\omega_i=0.012$ (lines marked with +).

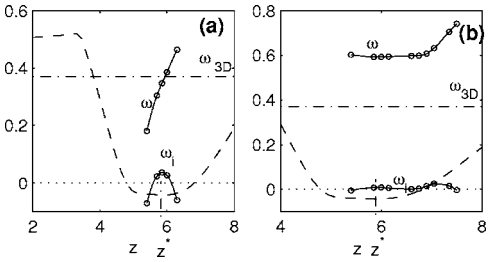

FIG. 28. Real part, ω, and imaginary part, ω_i, of the local absolute frequency as functions of z for case IV and two values of n: (a) $n=1$, and (b) $n=2$. The circles mark the actual computed points. The dashed-dotted line represents ω_{3D}, and the dashed line corresponds to the minimum value of the axisymmetric axial velocity as a function of z.

these saddle points in the dispersion relation are found. Note that only five of these cases correspond to absolute instabilities, those for which the imaginary part of the frequency is positive ($\omega_i^* \geq 0$). As an illustration, Fig. 26 shows the coalescence of two spatial branches in a saddle point of the dispersion relation for case III with $n=1$. We have plotted the evolution of the branches as ω_i is varied in the (α,ω), and in the (γ,ω) planes. It is seen how two spatial branches with $\omega_i=0$ (represented with circles) merge at a saddle point when ω_i is increased up to $\omega_i=+0.012$ (represented with the symbol "+" in the figure), indicating the presence of an absolute instability with a critical frequency $\omega^* \sim 0.435$. This critical frequency, and the specific azimuthal wave number for which we have found this absolute instability ($n=1$), agree pretty well with the numerical simulation reported in Sec. IV B, where $\omega_{3D} \sim 0.44$, and the 3D visualization of Fig. 13 indicates that the mode with $n=1$ is the dominant one in this case III.

In order to investigate what happens to the critical values of this absolute instability if we select another z station, we have carried out the local stability analysis in other sections of the pipe. Figure 27 shows the real part, ω, and the imaginary part, ω_i, of the local absolute frequency as functions of z for case III with $n=1$. Note that the flow is absolutely unstable ($\omega_i>0$) only in a narrow region close to $z=z^* \simeq 5.4$, and that there exists an excellent agreement between the local frequency at z^* and the global frequency ω_{3D} of the 3D simulation (dashed line).

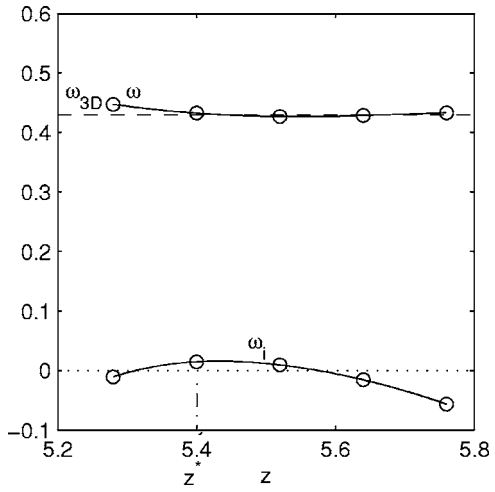

FIG. 27. Real part, ω, and imaginary part, ω_i, of the local absolute frequency as functions of z for case III with $n=1$. The circles mark the actual computed points. The dashed line corresponds to the value of the global frequency, ω_{3D}, obtained from the 3D simulation. The location $z=z^*$ is also marked.

The situation is similar for cases IV and V, where the numerical frequencies obtained in the 3D numerical simulations agree very well with the critical frequencies found from the stability analysis at $z=z^*$ for perturbations with $n=1$. For these two cases, Table I shows that there exist two additional absolute instabilities: one with $n=2$ for case IV, and another one with $n=-1$ for case V. However, the values of ω_i^* corresponding to these two absolute instabilities are smaller than the values of ω_i^* for the main absolute instabilities with $n=1$. In fact, the 3D simulations for the cases III, IV, and V suggest that only the absolute instabilities found here for $n=1$ are the responsible ones for the temporal evolution of the 3D flow.

We have also analyzed the absolute instability of the flow at different axial locations in these cases. For example, Fig. 28 shows ω and ω_i as functions of z for case IV and the two values of n for which the flow is absolutely unstable at $z=z^*$, namely $n=1$ and $n=2$. For $n=1$ the situation is similar to that represented in Fig. 27: the flow is absolutely unstable in a narrow region close to $z=z^* \simeq 5.85$ and there exists an excellent agreement between the local frequency at that station and the global frequency ω_{3D} of the 3D simulation [see Fig. 28(a)]. However, the situation is quite different for $n=2$ [Fig. 28(b)]. In this case there are two regions where the flow is absolutely unstable ($\omega_i>0$), one inside the breakdown bubble and another one in the wake just behind it. In order to better appreciate this fact we have included in the figures (with dashed lines) the minimum axial velocity at each z station, $\min_r[w_o(z,r)]$. A similar pattern, with two pockets of absolute instabilities, one inside the breakdown bubble and the other one in the wake, has been recently reported in open flows by Gallaire *et al.*[20] In our case, none of the absolute frequencies associated with this mode $n=2$ agree with the global frequency of the 3D simulation. Actually, the largest absolute ω_i for $n=2$ is not attained near $z=z^*$, but just behind the breakdown bubble [see Fig. 28(a)]. Yet $\omega_{i,\max}^{n=2} \simeq 0.025825$ is smaller than $\omega_{i,\max}^{n=1} \simeq 0.0435$ [Fig. 28(a) and Table I].

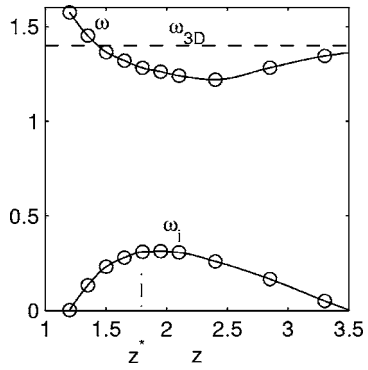

FIG. 29. Real part, ω, and imaginary part, ω_i, of the local absolute frequency as functions of z for case V with $n=1$. The dashed line marks the value of the global frequency, ω_{3D}, obtained from the 3D simulation. The location $z=z^*$ is also marked.

As discussed above for cases III and IV with $n=1$, we have also found a unique region of absolute instability for the most unstable mode for case V, which is also very close to the z station where the axial velocity presents a minimum value inside the breakdown bubble (see Fig. 29). As a difference with cases III and IV, the frequency ω_{3D} found in the 3D numerical simulations does not corresponds exactly to the largest absolute growth rate, but corresponds to a z station slightly upstream of z^*, while the location of the largest ω_i is a bit downstream of z^*. It is worth noticing that in this case V, with a wake-like velocity profile at the inlet, the absolute growth rates are much larger than in the previously discussed cases.

Let us finish with the discussion of the stability results for case II, which is slightly different to the previous ones. The local stability analysis at $z=z^*$ shows that there exists an absolute instability for $n=2$ (see Table I), with a critical frequency $\omega^* \sim 0.43$. The complementary analysis of the absolute instability of the flow at different axial locations for this case is shown in Fig. 30. Note that, although the largest absolute frequency, $\omega_{i,\max}^{n=2}$, is not attained at $z=z^*$, but at a slightly downstream position, there exists again an excellent agreement between the local frequency at z^* and the global frequency ω_{3D} of the 3D numerical simulation once the periodic flow is fully developed. This case is particularly interesting because the long time amplitude of the 3D waves observed in the 3D simulations does not correspond to the mode $n=2$, but to the mode $n=1$. In fact, the temporal evolution of the 3D flow shows that, at the initial stages, the mode with $n=2$ is the dominant one [see Figs. 8(a) and 9], just as the local stability analysis predicts, with a frequency of the oscillations at $t=2100$ given by $\omega_{3D}^{t=2100} \simeq 0.53$ [see inset in Fig. 8(a)], which coincides with the critical frequency of the local stability analysis at the z station where $\omega_{i,max}^{n=2}$ is attained (see Fig. 30). However, for larger times, the amplitude of the mode with $n=2$ decays, while the amplitude of mode with $n=1$ increases drastically, becoming the dominant one in the 3D simulations [see Figs. 8(a) and 10]. The final frequency of the flow coincides however with the frequency obtained from the stability analysis for the mode $n=2$ at $z=z^*$. All this suggests that nonlinear effects, that are obviously not taken into account in the linear stability analysis, may account for this change in the 3D structure of the flow from the mode with $n=2$ to the mode with $n=1$, once the first absolute instability with $n=2$ predicted by the local stability analysis develops in the flow.

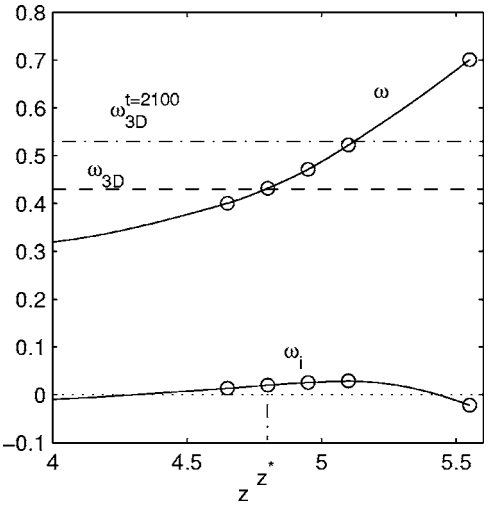

FIG. 30. Real part, ω, and imaginary part, ω_i, of the local absolute frequency as functions of z for case II with $n=2$. The dashed line marks the value ω_{3D} of the frequency obtained from the 3D numerical simulation for large times, while the dotted-dashed line marks the value $\omega_{3D}^{t=2100}$ of the frequency of the mode $n=2$ at its initial stages [$t=2100$; see inset in Fig. 8(a)].

VI. CONCLUSIONS

Three-dimensional and axisymmetric numerical simulations of the incompressible Navier-Stokes equations have been conducted to study the appearance and development of vortex breakdown in a family of columnar vortex flows inside a straight pipe without wall friction for several values of the Reynolds number. Both types of numerical simulations (axisymmetric and 3D) show that the columnar flow evolves towards an axisymmetric flow with a closed region of reverse flow if the relative strength of the swirl is sufficiently high. This means that, in the 3D scenario considered in this work, vortex breakdown can be viewed as a transition from a columnar axisymmetric swirling flow to a basic form of vortex breakdown which is axisymmetric ("bubble" breakdown). However our numerical simulations suggest that these axisymmetric "bubble" breakdown structures are unstable under infinitesimal, nonaxisymmetric perturbations if the Reynolds number is large enough. Thus, a transition to helical vortex breakdown modes is observed in the 3D simulations after the axisymmetric bubble structure is formed. The final solution at large time is a superposition of a steady axisymmetric flow and a helicoidal, and/or double-helicoidal, standing waves with a characteristic frequency of oscillation. We have also analyzed the role of the swirl parameter S, and of the jet- or wake-like nature of the axial velocity profile selected at the inlet of the pipe (characterized by the parameter a) in the development of these helical structures. The numerical simulations demonstrate that the frequency of the helical flows increases with the swirl parameter S (see Fig. 20). For jet-like velocity profiles at the inlet

($a<1$), the 3D evolution of the flow preserves the region of reverse flow near the entrance of the pipe, which remains almost axisymmetric, while for wake-like inlet flows ($a>1$), the region of reverse flow near the entrance disappears. The helicoidal winding sign of the wakes found in this work ($n>0$) agrees with the reported by Ruith *et al.*[14] in open vortices. In both cases, all the waves found in the 3D numerical simulations wind in opposite direction to the main flow.

We show here that the development of the helicoidal vortex breakdown structures in the flow is caused by a pocket of absolute instability inside the axisymmetric bubble of recirculating flow formed at the initial stages of the evolution of the flow. By means of a simple spatial, linear stability analysis carried out locally at the section where the basic axisymmetric flow present a (negative) minimum in the axial velocity at the axis, we have first shown that no 3D wakes develop when the flow is stable or just convectively unstable at these axial locations. This situation occurs for relatively low Reynolds numbers (case I considered in this work). When the Reynolds number is large enough, we have related the frequencies and the dominant azimuthal wave numbers observed in the 3D simulations with the critical frequencies, and the corresponding azimuthal wave numbers, of the absolute instabilities found at these axial stations. Although we have not make an exhaustive analysis owing to the enormous computational effort required by each 3D numerical simulation, the results are quite encouraging: in all the four cases where a helicoidal structure is found in the numerical simulation, the local stability analysis predicts with pretty good precision the frequency of the oscillations in the standing lee wave, and the value of the dominant azimuthal wave number. In one of the cases considered (case II), this good agreement is found only at the initial stages of the 3D evolution of the flow; afterwards, the flow evolves "nonlinearly" to a different helical structure which, obviously, cannot be predicted by the present linear stability analysis. But, surprisingly, the final frequency of the flow coincides with the frequency obtained from the stability analysis. It is interesting to emphasize here that the stability analyses are performed *locally* at the axial stations where the axial velocity presents a minimum (negative) value inside the bubble or recirculating flow formed by the initial axisymmetric vortex breakdown. To our knowledge, no such a simple criterion to predict 3D vortex breakdown structures, nor its detailed development from an axisymmetric form of vortex breakdown, have been previously reported, though the relation between vortex breakdown and absolute instabilities has been extensively debated for several types of swirling flows.[14,31–35]

Similar results, but in the context of bluff-body wakes, and considering the stability analysis in a finite region inside the near field of the wake just behind the body, have been recently reported by Pier and Huerre,[17,18] and by Sevilla and Martinez-Bazan,[36] among others. Finally to mention the recent work by Gallaire *et al.*,[20] where similar ideas are developed for open vortices. However, in contrast to the present results, these authors find two pockets of absolute instability for the dominant mode, one in the breakdown bubble and the other one in the wake behind it. Here, in all the cases considered, there is an unique region of absolute instability for the dominant mode inside the breakdown bubble, with the most absolutely unstable station close to the location where the axial velocity of the axisymmetric flow presents its minimum value ($z=z^*$). This criterion for the frequency selection based on the highest absolute growth rate was first proposed by Pierrehumbert[19] in the context of baroclinic instabilities, and differ from that given by Pier and Huerre[17,18] based on the frequency at the convective/absolute transition station. However, the frequency predictions by these two criteria are in reasonable agreement in the present problem due to the fact that all the frequencies within the pockets of absolute instability are in a relatively narrow range.

ACKNOWLEDGMENTS

This work has been supported by the Ministerio de Educación y Ciencia of Spain through Grants No. DPI2002-04305-C02-02 and No. FIS04-00538. The authors thank the anonymous referees for their valuable comments which have improved the quality of the paper.

[1] M. G. Hall, "Vortex breakdown," Annu. Rev. Fluid Mech. **4**, 195 (1972).
[2] T. Sarpkaya, "On stationary and travelling vortex breakdowns," J. Fluid Mech. **45**, 545 (1971).
[3] S. Leibovich, "The structure of vortex breakdown," Annu. Rev. Fluid Mech. **10**, 221 (1978).
[4] M. P. Escudier, "Vortex breakdown: observations and explanations," Prog. Aeronaut. Sci. **25**, 189 (1988).
[5] O. Lucca-Negro and T. O'Doherty, "Vortex breakdown: a review," Prog. Energy Combust. Sci. **27**, 431 (2001).
[6] J. D. Buntine and P. G. Saffman, "Inviscid swirling flows and vortex breakdown," Proc. R. Soc. London, Ser. A **449**, 139 (1995).
[7] S. Wang and Z. Rusak, "The dynamics of a swirling flow in a pipe and the transition to axisymmetric vortex breakdown," J. Fluid Mech. **340**, 177 (1997).
[8] R. Fernandez-Feria and J. Ortega-Casanova, "Inviscid vortex breakdown models in pipes," ZAMP **50**, 698 (1999).
[9] P. S. Beran and F. E. C. Culick, "The role of nonuniqueness in the development of vortex breakdown in tubes," J. Fluid Mech. **242**, 491 (1992).
[10] J. M. Lopez, "On the bifurcation structure of axisymmetric vortex breakdown in a constricted pipe," Phys. Fluids **6**, 3683 (1994).
[11] Z. Rusak and J. H. Lee, "The effect of compressibility on the critical swirl of vortex flows in a pipe," J. Fluid Mech. **461**, 301 (2002).
[12] M. A. Herrada, M. Pérez-Saborid, and A. Barrero, "Vortex breakdown in compressible flows in pipes," Phys. Fluids **15**, 2208 (2003).
[13] J. C. Tromp and P. S. Beran, "The role of nonuniqueness axisymmetric solutions in 3-d vortex breakdown," Phys. Fluids **9**, 992 (1997).
[14] M. R. Ruith, P. Chen, E. Meiburg, and T. Maxworhy, "Three-dimensional vortex breakdown in swirling jets and wakes: direct numerical similation," J. Fluid Mech. **486**, 331 (2003).
[15] F. Gallaire and J.-M. Chomaz, "Mode selection in swirling jet experiments: a linear stability analysis," J. Fluid Mech. **494**, 223 (1995).
[16] H. Liang and T. Maxworthy, "An experimental investigation of swirling jets," J. Fluid Mech. **525**, 115 (2005).
[17] B. Pier and P. Huerre, "Nonlinear self-sustained structures and fronts in spatially developing wake flows," J. Fluid Mech. **435**, 145 (2001).
[18] B. Pier, "On the frequency selection of finite-amplitude vortex shedding in the cylinder wake," J. Fluid Mech. **458**, 407 (2002).
[19] R. T. Pierrehumbert, "Local and global baroclinic instability of zonally varying flow," J. Atmos. Sci. **41**, 2141 (1984).
[20] F. Gallaire, M. R. Ruith, E. Meiburg, J. M. Chomaz, and P. Huerre, "Spiral vortex breakdown as a global mode," J. Fluid Mech. **549**, 71 (2006).
[21] J. H. Faler and S. Leibovich, "An experimental map of the internal structure of a vortex breakdown," J. Fluid Mech. **86**, 313 (1977).
[22] G. K. Batchelor, "Axial flow in trailing line vortices," J. Fluid Mech. **20**, 645 (1964).
[23] *Fluid Vortices*, edited by S. I. Green (Kluwer, Dordrecht, 1995).

[24]S. A. Orszag, "Fourier series on spheres," Mon. Weather Rev. **102**, 56 (1974).
[25]J. M. Lopez, F. Marques, and J. Shen, "An efficient spectral-projection method for the Navier-Stokes equations in cylindrical geometries ii. three dimensional cases," J. Comput. Phys. **176**, 401 (2002).
[26]R. E. Lynch, J. R. Rice, and D. H. Thomas, "Direct solution of partial differential equations by tensor product methods," Numer. Math. **6**, 85 (1964).
[27]C. Canuto, M. Y. Hussaini, A. Quarteroni, and T. A. Zang, *Spectral Methods in Fluid Dynamics* (Springer-Verlag, New York, 1988).
[28]T. J. Bridges and P. J. Morris, "Differential eigenvalue problems in which the parameter appears nonlinearly," J. Comput. Phys. **55**, 437 (1984).
[29]P. Huerre and P. A. Monkewitz, "Local and global instabilities in spatially developing flows," Annu. Rev. Fluid Mech. **22**, 473 (1990).
[30]J.-M. Chomaz, "Global instabilities in spatially developing flows: nonnormality and nonlinearity," Annu. Rev. Fluid Mech. **37**, 357 (2005).
[31]I. Delbende, J.-M. Chomaz, and P. Huerre, "Absolute/convective instabilities in the batchelor vortex: A numerical study of the linear impulse response," J. Fluid Mech. **355**, 229 (1998).
[32]C. Olendraru, A. Sellier, M. Rossi, and P. Huerre, "Inviscid instability of the batchelor vortex: Absolute-convective transition and spatial branches," Phys. Fluids **11**, 1805 (1999).
[33]T. Loiseleux, I. Delbende, and P. Huerre, "Absolute and convective instabilities of a swirling jet/wake shear layer," Phys. Fluids **12**, 375 (2000).
[34]X.-Y. Yin, D.-J. Sun, M.-J. Wei, and J.-Z. Wu, "Absolute and convective character of slender viscous vortices," Phys. Fluids **12**, 1062 (2000).
[35]C. Olendraru and A. Sellier, "Viscous effects in the absolute-convective instability of the Batchelor vortex," J. Fluid Mech. **459**, 371 (2002).
[36]A. Sevilla and C. Martinez-Bazan, "Vortex shedding in high Reynolds number axisymmetric bluff-body wakes: Local linear instability and global bleed control," Phys. Fluids **16**, 3460 (2004).